This is to certify that the
thesis entitled

IMPROVING THE CHARACTERIZATION OF BREAST LESIONS USING DCE-MRI AND DTI

presented by

TOBIAS HAHN

has been accepted towards fulfillment
of the requirements for the

M.S. degree in PHYSICS

Major Professor's Signature

7-29-08

Date

IMPROVING THE CHARACTERIZATION OF BREAST LESIONS USING DCE-MRI AND DTI

By

Tobias Hahn

A THESIS

Submitted to
Michigan State University
in partial fulfillment of the requirements
for the degree of

MASTER OF SCIENCE

Department of Physics

2008

Abstract

IMPROVING THE CHARACTERIZATION OF BREAST LESIONS USING DCE-MRI AND DTI

By

Tobias Hahn

Breast magnetic resonance imaging (MRI) has evolved to be accepted as an important lesion diagnosis technique, providing higher sensitivities than other techniques such as mammography. However, like the other techniques, one main limitation is still a relatively low specificity. The main goal of this study was to reduce the Type I error of breast MRI via investigating new methods for the analysis of dynamic contrast-enhanced (DCE) breast MRI and breast diffusion tensor imaging (DTI). A software for an automatic detection of breast lesions was developed, tested and demonstrated to be reliable for the detection of the lesion margin. Then we investigated the kinetic features of breast lesions and introduced the slope angle as a measure for characterizing the kinetic behavior. The study showed that the slope angle clearly separated our sample into two groups of benign and malignant and consequently could be used to significantly reduce the Type I error. Finally, we examined the usage of breast DTI for improving the characterization of breast lesions. We found no significant difference in mean diffusivity between the benign and the malignant group. However, we found a significant difference in relative change of the mean diffusivity, which could be used as an additional measure for improving the characterization of breast lesions.

ACKNOWLEDGMENTS

The research project described in this thesis would not have been possible without the support from many people. I am deeply grateful for the incomparable support that I received from my adviser, Prof. Jie Huang, during my research on this project. I want to express my thankfulness to Prof. Wolfgang Bauer for providing the opportunity to spend an inspiring and fruitful time at Michigan State University. I am very grateful for the technical and financial support granted by Prof. E. James Potchen and the Department of Radiology at Michigan State University. I want to thank Lori Hoisington and Prof. Kevin Berger for their commitment in this research project. Thanks to Prof. James Lyon for reading the manuscript and helpful suggestions. I acknowledge the support of the Studienstiftung des deutschen Volkes.

I especially want to thank Emanuel Gavartin, Luis Carlos Reyes, my family and in particular Dr. Matthias Hahn for innumerable ways of supporting and motivating me.

Soli Deo Gloria.

Contents

List of Tables

List of Figures

Figures in this thesis are presented in color.

Chapter 1

Introduction

Breast cancer, the most frequent cancer among women [20], is an increasing threat as the cases per year increase [12], causing nearly 1% of all deaths worldwide in 2005 [20]. In recent years, breast magnetic resonance imaging (MRI) has evolved into an established technique for supplementing other lesion diagnosis methods such as mammography and breast ultrasound. One of the big advantages of breast MRI, in comparison to other techniques, is its high sensitivity, being $27 - 36\%$ more sensitive than mammography [8]. With current technology, the sensitivity of breast MRI almost reached 100% [26]. One of the major concerns about breast MRI, however, is its low specificity [8]: The *Type 1 error*, denoting the false positive rate, is still significant for breast MRI, where the exact specificity values vary a lot between different studies [26]. Due to small specificity values, many biopsies are recommended for what prove to be truly benign lesions. Each biopsy, in return, leads to psychological costs for women. An unnecessary biopsy should be avoided, since it is an invasive procedure with possible side effects such as infections, altered breast appearance etc. The crucial task, therefore, is to maintain a high sensitivity, while reducing the Type 1 error and with it the number of unnecessary biopsies. In this work, different approaches on the basis of dynamic contrast-enhanced (DCE) breast MRI and breast diffusion tensor imaging (DTI) are described to tackle this task.

Chapter 2

Overview of Magnetic Resonance Imaging

2.1 Historical Overview

MRI is a non-invasive imaging technique that has been developed during the last century, whose potential, however, still seems to be far from being fully revealed.

In contrast to other imaging techniques, such as X-ray imaging, MRI is an unequally more sophisticated method. Where for X-ray less than one year passed between the first observations of the underlying physical principal and the first image taken (both by Wilhelm Conrad Roentgen in 1895) for MRI this was a matter of decades.

In 1930, Isidor Isaac Rabi conducted experiments that led to a "resonance method for recording the magnetic properties of atomic nuclei."[1] After having developed a technique to measure the magnetic moments of the nuclei of a molecular beam to high precision, he introduced - according to suggestions by the Dutch physicist Cornelius J. Gorter - a method to flip nuclear spins of a sample by applying radio waves to this sample. These methods turned out to be harbingers of the upcoming MRI technology.

[1] The Nobel Prize Committee, 1944.

In 1945 and 1946 Edward Purcell and Felix Bloch independently observed nuclear magnetic resonance in bulk matter. Molecular resonance spectroscopy (MRS) was a fruit of their discoveries; this new technique revealed information about how much of what kind of molecules was included in the examined sample by exciting the molecular spins according to their resonance condition. Only in 1973, the known physical principals were applied for imaging by Paul C. Lauterbur and Peter Mansfield, an accomplishment for which they were awarded the 2003 Nobel Prize in Physiology or Medicine.

2.2 Nuclear Magnetic Resonance

Magnetic resonance imaging is primarily based on the magnetic field interactions with the nuclei of a sample[2].

According to Maxwell's theory of magnetic fields, spinning charges induce a magnetic field and a magnetic moment, respectively. With regard to their specific quark composition, we can consider both protons and neutrons as spinning charges, having a "spin" angular momentum $\vec{S}$ that induces a spin magnetic moment $\vec{\mu}$ with

$$\vec{\mu} = g\frac{q}{2m}\vec{S} = \gamma\vec{S}. \tag{2.2.1}$$

Hereby, g denotes the particle specific g-factor, γ the gyromagnetic ratio and m and q the mass and charge of the particle, respectively. According to their specific proton/neutron composition, nuclei have a specific spin inducing a magnetic moment that interacts with external magnetic fields[3].

[2]There are certain techniques that make use of the magnetic field interactions with other particles, such as Electron Spin Resonance Enhanced Magnetic Resonance Imaging (ESREMRI). They are, however, not subject of this work.

[3]The spin concept is of fundamentally quantum mechanical nature. It is however more intuitive to regard the physical principals of MRI from a classical point of view and it can indeed be shown that the classical description leads to the same results as the Quantum mechanical approach, see e.g. [7]. Therefore we want to treat the spin as a classical angular momentum.

A magnetic moment $\vec{\mu}$ in an external magnetic field $\vec{B_0}$ is affected by a torque $\vec{N}$, given by

$$\vec{N} = \vec{\mu} \times \vec{B_0}, \tag{2.2.2}$$

where the index 0 denotes that the magnetic field is static. This formula can be derived for the classical magnetic moment of a current loop. For magnetic moments that are not associated with an angular momentum (like the magnetic moment given by a pair of magnetic charges with opposite sign, in analogy to an electric dipole moment given by two charges), the torque will simply lead to an alignment of the magnetic moment vector with the external magnetic field. A magnetic potential energy H, given by

$$H = -\vec{\mu} \cdot \vec{B_0}, \tag{2.2.3}$$

is associated with the torque that pushes the magnetic moment vector towards an alignment with the magnetic field. Following the natural tendency to be in a state of lowest possible energy, the preferred state, $\vec{\mu} \| \vec{B_0}$, has the lowest energy.

If the magnetic moment, however, is associated with an angular momentum - like in the case of a spin - the resulting torque on an unaligned magnetic moment leads to a *precession* of the magnetic moment around the $\vec{B_0}$ axis.

The fundamental equation of motion for the magnetic moment vector can be found using (2.2.2) and Newton's second law, according to which it can be derived that the torque is equal to the derivative of the angular momentum, yielding

$$\frac{d\vec{S}}{dt} = \frac{1}{\gamma}\frac{d\vec{\mu}}{dt} = \vec{N} = \vec{\mu} \times \vec{B}$$

$$\Rightarrow \boxed{\frac{d\vec{\mu}}{dt} = \gamma \vec{\mu} \times \vec{B}}. \tag{2.2.4}$$

We want to consider now the case of a magnetic moment vector, which is aligned with the external magnetic field, and introduce the principals of Rabi's spin flip method that has already been mentioned above: Spins can be brought out of the alignment with the

$\vec{B_0}$ axis into the transverse plane by applying energy to the spins using a radio-frequency electromagnetic radiation pulse. The tipping is most effective if the radio-frequency (RF) pulse is tuned to the specific precession frequency of the spins, i.e., if the excitation happens on-resonant[4]. A famous analogue for this excitation process is the swing, which is most effectively excited if an external force excites the swing with the swing specific frequency. The specific precession frequencies of the spins are the well-known *Larmor frequencies* ω_0, which are given by

$$\omega_0 = \gamma B_0. \tag{2.2.5}$$

For an on-resonant excitation, the pulse energy is given by $\hbar\omega_0$, which corresponds to the energy difference between the excited state and the ground state. In the absence of a magnetic field, thermal agitation leads to a random orientation of the magnetic moments. Generally speaking, for a given small volume, the microscopic random orientation results in a zero macroscopic sum of the magnetic moments. In the presence of an external magnetic field, however, a preferred direction is given as the magnetic field direction and in the equilibrium state the number of ground states (N_-) prevails the number of excited states (N_+) according to the Boltzmann distribution,

$$\frac{N_-}{N_+} = exp\left(\frac{\hbar\omega_0}{kT}\right), \tag{2.2.6}$$

with the thermal energy $E_T = kT$ being usually much larger than $\hbar\omega_0$. Still, no direction in the plane perpendicular to the external magnetic field is preferred, leading to a zero transverse bulk magnetization. However, the slight excess of aligned spins over unaligned spins leads to a non-zero bulk magnetization in the direction of the B_0-field. We introduce the *magnetization* $\vec{M}$ as the magnetic moment per volume V, where V is assumed to be small enough so that external fields are to a good approximation constant over V [7]:

$$\vec{M} = \frac{1}{V}\sum_{i \in V} \vec{\mu_i},$$

[4]Less power is required to flip spins if the exciting field rotates in the same way as the precessing magnetic moment vector. Therefore for MR applications the commonly used radio frequency field is left-circularly polarized.

where the index i denotes the different protons. A first order approximation of (2.2.6) for a spin $\frac{1}{2}$ system[5] returns the *Curie Law*

$$M_0 \propto \frac{B_0}{T}, \tag{2.2.7}$$

revealing the dependence of the equilibrium magnetization M_0 on the B_0-field and the temperature.

In the absence of interactions between the spins and interactions between the spins and their surrounding lattice, the fundamental equation of motion (2.2.4) can directly be adapted for a bulk magnetization system that has been tipped away from the equilibrium state:

$$\frac{d\vec{M}}{dt} = \gamma \vec{M} \times \vec{B}_0. \tag{2.2.8}$$

It is $\vec{M}_{\|} \times \vec{B}_0 = 0 \Rightarrow \frac{d\vec{M}_{\|}}{dt} = 0$, from which follows that $\vec{M}_{\|}$ remains unchanged, where $\vec{M}_{\|}$ is the longitudinal magnetization component. For the transverse component, $\vec{M}_{\perp} = \vec{M}_x + \vec{M}_y$, we get $\vec{M}_{\perp} \times \vec{B}_0 \neq 0$, however the magnitude of $M_{\perp}$ does not change, but the transverse magnetization precesses around $\vec{B}_0$ with the Larmor frequency $\omega_0 = \gamma B_0$.

However, due to interactions of the system with its surrounding lattice, the longitudinal component of the bulk magnetization recovers, and due to inner-system spin-spin-interactions, the transverse component decays. Assuming that the external magnetic field is applied in z-direction, the components obey the equations given in (2.2.9) and (2.2.10):

Spin-lattice interactions lead to

$$\frac{dM_z}{dt} = \frac{1}{T_1}(M_0 - M_z) \tag{2.2.9}$$

and *Spin-spin-interactions* change the perpendicular component of (2.2.8) into

$$\frac{d\vec{M}_{\perp}}{dt} = \gamma \vec{M}_{\perp} \times \vec{B}_0 - \frac{1}{T_2}\vec{M}_{\perp}, \tag{2.2.10}$$

where $\perp$ denotes the magnetization perpendicular to the $\vec{B}_0$ axis with $\vec{M}_{\perp} = \vec{M}_x + \vec{M}_y$.

[5]In this description we want to stick to spin $\frac{1}{2}$ systems. The most common NMR-active nuclei ^1H, ^{13}C or ^{19}F are all spin $\frac{1}{2}$ systems.

Equation (2.2.10) can be explained by the process of dephasing: As time goes by, the spin vectors of the spins in the sample start pointing in different directions, caused by the mutual spin interactions - and according to (2.2.7) $\vec{M}$ decreases.

(2.2.9) and (2.2.10) can be combined, resulting in the *Bloch equation*:

$$\boxed{\frac{d\vec{M}}{dt} = \gamma\vec{M} \times \vec{B} + \frac{1}{T_1}(M_0 - M_z)\hat{z} - \frac{1}{T_2}\vec{M}_\perp.} \tag{2.2.11}$$

In addition to spin-spin interactions being reflected in $T2$, magnetic field inhomogeneities also induce a dephasing. A new parameter, $T2^*$, is introduced according to

$$\frac{1}{T2^*} = \frac{1}{T2} + \frac{1}{T2'},$$

where $T2'$ takes into account the field inhomogeneity-induced dephasing. For the following, $T2$ has to be replaced by $T2^*$ in the case of present field inhomogeneities.

The solution to (2.2.11) can be written down for each component, given $\vec{B} = B_0\hat{z}$ and using (2.2.5):

$$M_x(t) = e^{-t/T_2}\left(M_x(0)\cos(\omega_0 t) + M_y(0)\sin(\omega_0 t)\right) \tag{2.2.12}$$

$$M_y(t) = e^{-t/T_2}\left(M_y(0)\cos(\omega_0 t) - M_x(0)\sin(\omega_0 t)\right) \tag{2.2.13}$$

$$M_z(t) = M_z(0)e^{-t/T_1} + M_0(1 - e^{-t/T_1}). \tag{2.2.14}$$

Defining the complex transverse magnetization $M_+ = M_x + iM_y$ yields:

$$M_+(t) = e^{-i\omega_0 t - t/T_2}M_+(0)^6. \tag{2.2.15}$$

2.3 MR signal detection

Mostly, a single coil around the object of interest to be scanned (*subject*) acts at the same time as a transmitter and receiver coil (= *transceiver*) for the radio frequency pulses. We can tip the magnetization vector away from the $\vec{B_0}$-direction by applying a radio frequency

[6]For derivations of the above equations see [7].

pulse onto the subject using the transceiver. Depending on how long the RF pulse is applied and which amplitude is used, respectively, we can tip the vector by an arbitrary angle.
According to Faraday's law of induction, the precessing magnetization vector induces a voltage inside the transceiver coil, given by

$$U_{ind} = -\frac{d\Phi}{dt} = -\frac{d}{dt}\int_{\text{coil area}} \vec{B} \cdot d\vec{A} \tag{2.3.16}$$

with Φ being the magnetic flux and A the surface vector of the area regarded. This integral can be transformed - according to the principle of reciprocity - into a volume integral over the magnetization times the magnetic field per unit current, $\vec{B}^r = \vec{B}/I$, that would excite the magnetization of the sample if $B^r \cdot I$ was used for the excitation [11]:

$$U_{ind} = -\frac{d}{dt}\int \left(\vec{M} \cdot \vec{B}^r\right) d^3r. \tag{2.3.17}$$

Equation (2.3.17) makes clear the dependence of the induced voltage on the magnetization vector.

The measured signal is proportional to U_{ind}, whereat the proportionality factor depends on the measurement device. We insert the solutions (2.2.14) and (2.2.15) to the Bloch equation into (2.3.17). Since usually $\omega_0 \gg 1/T_1$ and $\omega_0 \gg 1/T_2$, the time derivatives in (2.3.17) - which we can take inside the integrand - of all exponentials that contain $1/T_1$ or $1/T_2$ terms can be neglected, comparing them to the time derivatives of the ω_0-dependent exponential functions. Therefore, the contribution of the longitudinal magnetization to the signal is negligible and this is why the transverse magnetization M_+ or its magnitude $M_\perp = \sqrt{M_x^2 + M_y^2}$ is also referred to as 'the signal'.
The *free induction decay, FID*, refers to the signal decay after an RF pulse. After applying such a pulse due to spin-spin interactions ($T2$) and field inhomogeneities ($T2'$) the transversal component of the magnetization vector decays and with it the signal, which is shown in Figure 2.1.

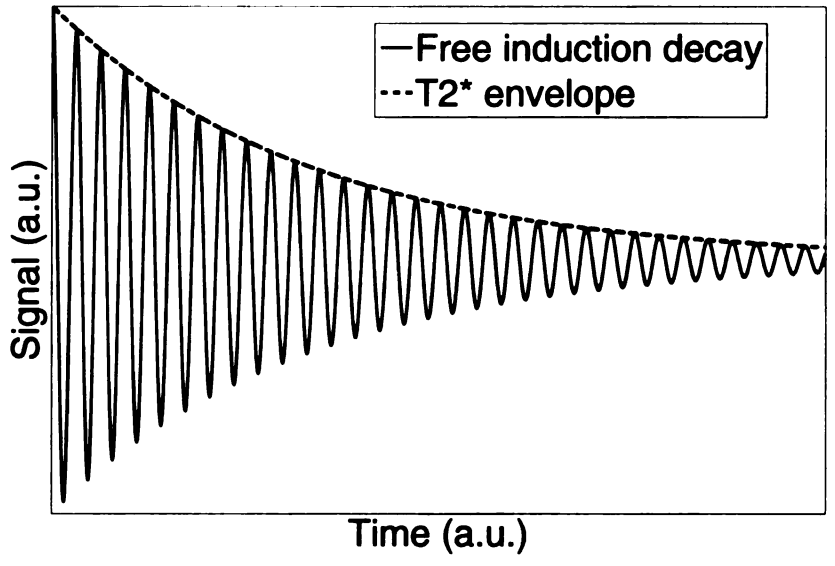

Figure 2.1. Free induction decay with T2* envelope for all spins precessing at the same Larmor frequency.

2.4 Signal spatial encoding and image reconstruction

Combining (2.3.17) and (2.2.15) yields for the signal s at time t:

$$s(t) = \int d^3r \rho(\vec{r}) e^{i\phi(\vec{r},t)} e^{-t/T_2^*}, \tag{2.4.18}$$

where $\phi(\vec{r}, t)$ is the accumulated phase at a certain position $\vec{r}$ at a given time t and ρ the effective spin density, which includes all sample specific scaling factors[7]. As long as the sampling time (or "data acquisition window") is small in comparison to $T2^*$, e^{-t/T_2^*} can be pulled out of the integral as a constant that we want to disregard in the following.

We want to consider a one-dimensional scenario and introduce a spatial linear gradient in z-direction in addition to the static magnetic field, giving

$$B_z(z,t) = B_0 + zG(t).$$

[7]The reader is referred to literature such as [7] for a detailed derivation.

The angular frequency of the spins changes according to

$$\omega(z,t) = \omega_0 \rightarrow \omega(z,t) = \omega_0 + \omega_G(z,t)$$
$$= \omega_0 + \gamma z G(t). \tag{2.4.19}$$

Given (2.4.19), we have developed a relation between the spatial position of the spins and their precession frequencies. The spins are said to be *frequency encoded* (in z-direction). (2.4.18) is changed to

$$s(t) = \int dz \rho(z) e^{i(\phi_G(z,t)+\phi_{const})} = \int dz \rho(z) e^{-i\int dt \omega(z,t)}$$
$$= \int dz \rho(z) \exp\left[i(-\gamma z \int_0^t dt' G(t') + \phi_{const})\right]. \tag{2.4.20}$$

ϕ_{const} denotes a constant phase offset, which can be disregarded at this point. Identifying

$$k(t) = \frac{\gamma}{2\pi} \int_0^t dt' G(t')$$

as the spatial frequency changes (2.4.20) into

$$s(k) = \int dz \rho(z) e^{-i2\pi k z} \tag{2.4.21}$$

and we recognize the measured signal as the Fourier transform of the spin density of the sample. In order to retrieve $\rho(z)$, we change k until the whole k-space is covered, and run the Fourier transform. In real MRI applications at least three different gradients have to be applied for two dimensional images: a *slice selection* gradient to determine the slice of interest and a *frequency-* and a *phase-* encoding gradient to cover the two-dimensional k-space[8].

2.5 The spin echo pulse sequence

In a spin echo pulse sequence - which was used for the acquisition of the below discussed DTI images (see chapter 6) - first a 90° pulse is applied, flipping the magnetization vector

[8]We refer the interested reader at this point to further reading such as [7, 2].

into the plane perpendicular to the external magnetic field and leading to a free induction decay as in Figure 2.1. The basic idea is now to undo the non-random dephasing due to field inhomogeneities, quantified by $T2'$, by applying a 180° pulse after a certain time when the signal has been reduced to a certain extent. We call this time τ. The pulse flips all spins in the plane $\perp \vec{B}$ by 180°, leading to a rephasing of the spins as if we did a time reversal. The signal is at maximum after the *echo time* $T_E = 2\tau$. Multiple 180° pulses can be applied, each after the *repetition time* T_R. Depending on the chosen T_E-and T_R-values, images with different *weighting* can be acquired[9].

The magnitude of the transverse magnetization for a sampling at the echo time T_E is given by

$$M_\perp(T_E) = M_0(1 - e^{-T_R/T_1})e^{-T_E/T_2}. \tag{2.5.22}$$

An illustration of a basic spin echo pulse sequence is given in 2.2. Figure 2.3 shows the signal time evolution for the sequence.

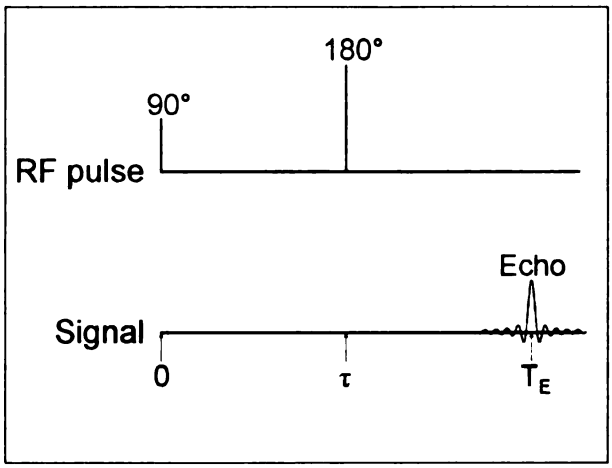

Figure 2.2. The basic spin echo pulse sequence.

[9]We refer the interested reader to pertinent literature, such as [7, 2, 27].

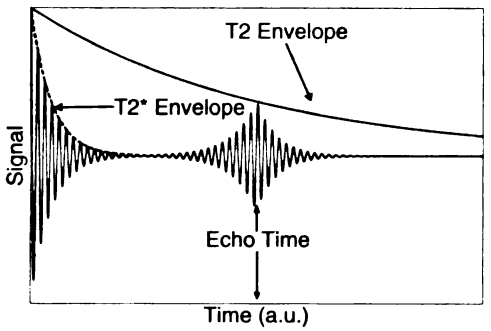

Figure 2.3. The signal of the spin echo pulse sequence.

2.6 The gradient-recalled echo pulse sequence

Multiple images, that have been used for this work, had been acquired using the below described dynamic contrast-enhanced imaging method (see chapter 2.7). This method uses not the spin echo, but the *gradient-recalled echo pulse sequence* to acquire the images. As the name implies, the echo in the gradient-recalled echo pulse sequence is obtained not by rephasing the spins using a 180° pulse, but using a gradient.

A variable flip angle can be chosen for the excitation. After exciting the system, a gradient (*spoiler*) is applied, which - according to (2.4.19) - changes the precession frequencies of the nuclei at different spatial locations. This way the spins dephase very quickly. After the dephasing induced by the spoiler, a different gradient (*rewinder*) is applied, whose magnetic field gradient points in the opposite direction than the field gradient of the spoiler. Naturally, the spins rephase again very quickly and a maximum signal intensity is achieved at the echo time T_E, when an echo signal was formed.

It is an advantage of the gradient-recalled echo pulse sequence that the rephasing process can be run much quicker than with the 180° pulse in the spin echo pulse sequence case. Smaller flip angles than 90° also speed up the sequence, since the repetition time T_R can be chosen smaller. Smaller flip angles also lead to a smaller energy deposit in the sample. However, there is no compensation for magnetic field inhomogeneities in the gradient-

recalled echo pulse sequence in contrast to the spin echo pulse sequence, where the $180°$ pulse compensates for field inhomogeneities. We characterize the signal decay by a new time constant $T2^{**}$, that takes into account all effects included in $T2$ and in addition the dephasing due to the field inhomogeneity given by the applied gradient. An illustration of the basic gradient-recalled echo pulse sequence is given in 2.4. Figure 2.5 shows the signal time evolution for the sequence.

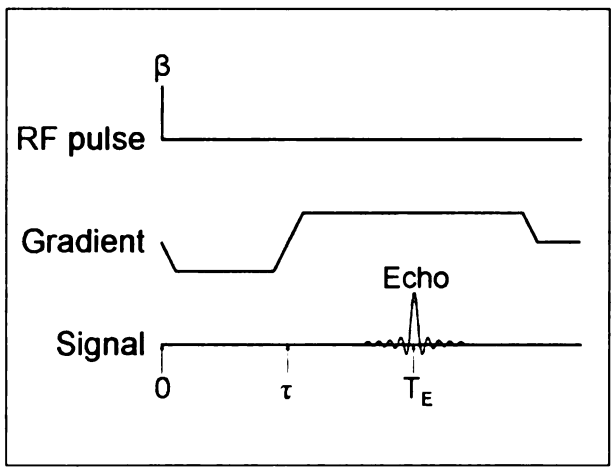

Figure 2.4. The basic gradient-recalled echo pulse sequence for a tip angle β.

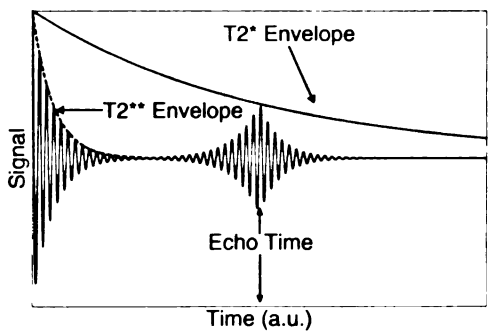

Figure 2.5. The signal of the gradient-recalled echo pulse sequence.

2.7 Principles of Dynamic Contrast-Enhanced MRI

Dynamic contrast-enhanced MRI allows for the study of signal intensity time courses by injecting an intravenous tracer, such as compounds of Gadolinium, into the patient's blood-stream. At room temperature, Gadolinium exhibits highly paramagnetic features, leading to reduced $T1$ and $T2$ values. In a $T1$-weighted image, a reduced $T1$ will result in a bright area. The awaited contrast enhancement shortly after the intravenous injection of a gadolinium chelate is broadly assumed by researchers to be a key for (breast) MR imaging [22]. Obtaining a series of post-contrast images after certain time intervals allows for the calculation of signal intensity curves (*kinetic curves*) for specific chosen regions of interest (*ROIs*). Examples of three distinct possible kinetic curves are given in Figure 2.6.

There is a physiological reasoning for an association of the shape of a kinetic curve for a specific lesion with its diagnosis. Most of the cancers demonstrate a rapid increase in gadolinium concentration after the injection of the tracer, most probably due to an increased vascularity (vessel density) in comparison to benign lesions or normal tissue. However, it is still not clear what exactly determines the degree of enhancement, since it has been shown that vessel density cannot be the only contributor [13]. The vascularity increase is due to an augmented growth of blood vessels (*angiogenesis*), which is necessary for tumor expansion. The growing capillaries have been shown to be leaky [13], leading to an accelerated extravasation of contrast material. Therefore wash-out curves are to a high extent associated with malignancy.

Aside the kinetic properties, lesion architecture can be used to set up criteria for the histological diagnosis. Among different features to look at, clear versus smooth borders and rim versus stippled regional enhancement are commonly examined features to distinguish between malignant and benign lesions [22].

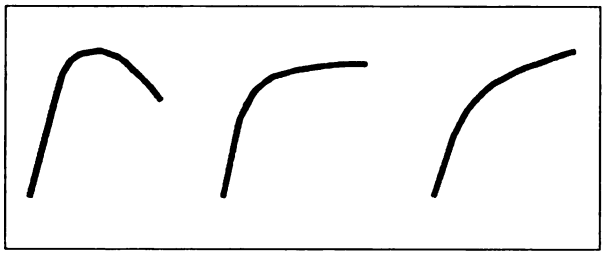

Figure 2.6. Different kinetic curve shapes. Left: Wash-out behavior. Center: Plateau behavior. Right: Persistence behavior.

2.8 Principles of Diffusion Tensor Imaging

Random molecular motion or Brownian motion causes matter transport from one part of a system to another part of the system. This process of matter transfer is called *Diffusion* [3]. Diffusion tensor imaging reveals quantitative information about the diffusion properties of the scanned sample. The most important diffusion properties include mean diffusivity and anisotropy, which have turned out to possibly constitute quantities to delineate between malignant and benign breast lesions [6, 21].

2.8.1 Physical background

Tissue in real cases is never uniform; diffusion is generally orientation dependent, given different concentration gradients in different directions. In this case the diffusion can be described by a second rank tensor

$$\boldsymbol{D} = \begin{bmatrix} D_{xx} & D_{xy} & D_{xz} \\ D_{yx} & D_{yy} & D_{yz} \\ D_{zx} & D_{zy} & D_{zz} \end{bmatrix}.$$

Fick's first law states that the transfer rate of diffusing matter - the diffusing flux $\vec{J}$ - is proportional to the macroscopic concentration gradient ∇C:

$$\vec{J} = -\boldsymbol{D}\nabla C. \tag{2.8.23}$$

$\boldsymbol{D}$ is assumed to be symmetric. This assumption is based on the reciprocity theorem and the principle of microscopic reversibility [18, 19], and is valid for microscopic systems. However, though dealing with macroscopic quantities, this assumption is also valid for the MRI applications described in this paper to a high accuracy, which can be verified by measuring all 9 diffusion coefficients and comparing the off-diagonal elements of $\boldsymbol{D}$. Since Diffusion is a measurable physical quantity, it has to be determined by real values. The Spectral Theorem tells us that any symmetric matrix with real entries can be diagonalized. The orientation independent eigenvalues (D_{11}, D_{22}, D_{33}) of the matrix $\boldsymbol{D}$ represent the diffusion coefficients in the principal diffusivity directions, which are given by the eigenvectors of $\boldsymbol{D}$.

2.8.2 Definitions

We define four invariants, I_1 (trace), I_2, I_3 (determinant) and I_4:

$$I_1 = D_{11} + D_{22} + D_{33} \tag{2.8.24}$$

$$I_2 = D_{11}D_{22} + D_{11}D_{33} + D_{22}D_{33} \tag{2.8.25}$$

$$I_3 = D_{11}D_{22}D_{33} \tag{2.8.26}$$

$$I_4 = D_{11}^2 + D_{22}^2 + D_{33}^2. \tag{2.8.27}$$

The first three invariants can be interpreted as physical quantities determining the shape of a "diffusion ellipsoid." This ellipsoid can be illustrated with the process of the diffusion of a spherical ink drop that is being placed inside a water volume: It will form an ellipsoid that spreads with time. I_1 would then describe the sum of the square of the radii of the ellipsoid, I_2 the square of its surface and I_3 the square of its volume [25].

The later used quantities *Fractional Anisotropy* (FA) and *mean diffusivity* ($\langle D \rangle$) are defined

as:

$$\mathrm{FA} = \sqrt{1 - \frac{I_2}{I_4}} \tag{2.8.28}$$

$$\langle D \rangle = \frac{I_1}{3}. \tag{2.8.29}$$

2.8.3 Measurement of the Diffusion Coefficients

Stejskal related the diffusion coefficients with the echo intensities [24] at the echo time T_E in a spin-echo experiment (see Figure 2.7) by

$$\frac{A(\vec{G})}{A(0)} = \exp(-\sum_{i,j=1}^{3} b_{ij} D_{ji}). \tag{2.8.30}$$

with

$$b_{ij} = \gamma^2 \left[\delta^2 \left(\Delta - \frac{\delta}{3} \right) + \frac{\epsilon^3}{30} - \frac{\delta \epsilon^2}{6} \right] G_i G_j \tag{2.8.31}$$

and the echo intensities

$$\begin{aligned} A(\vec{G}) &= \sqrt{\mathrm{Re}(m(\vec{G}))^2 + \mathrm{Im}(m(\vec{G}))^2} \text{ and} \\ A(0) &= \sqrt{\mathrm{Re}(m(0))^2 + \mathrm{Im}(m(0))^2}. \end{aligned} \tag{2.8.32}$$

We can also write this as

$$m(\vec{G}) = m(0) \exp(-\boldsymbol{b} : \boldsymbol{D}), \tag{2.8.33}$$

with $m = Ae^{i\phi}$ being the magnetization and $\vec{G}$ a given gradient at time T_E. ':' refers to the scalar generalized tensor product, which is defined as:

$$\boldsymbol{b} : \boldsymbol{D} = \sum_{i,j=1}^{3} b_{ij} D_{ji}.$$

For a derivation of (2.8.33) see [10].

According to (2.8.33), $\boldsymbol{D}$ attenuates the echo intensity.

Taking into account (2.8.30), one can acquire the different components of $\boldsymbol{D}$ by applying

gradients along different directions: Using a gradient pulse sequence with $\vec{G}$ having only a component in the x-direction for example leads to

$$\ln\left[\frac{A(\vec{G})}{A(0)}\right] = -b_{xx}D_{xx}$$

with the measurable quantities $A(\vec{G})$, $A(0)$ and the known quantity b_{xx}.

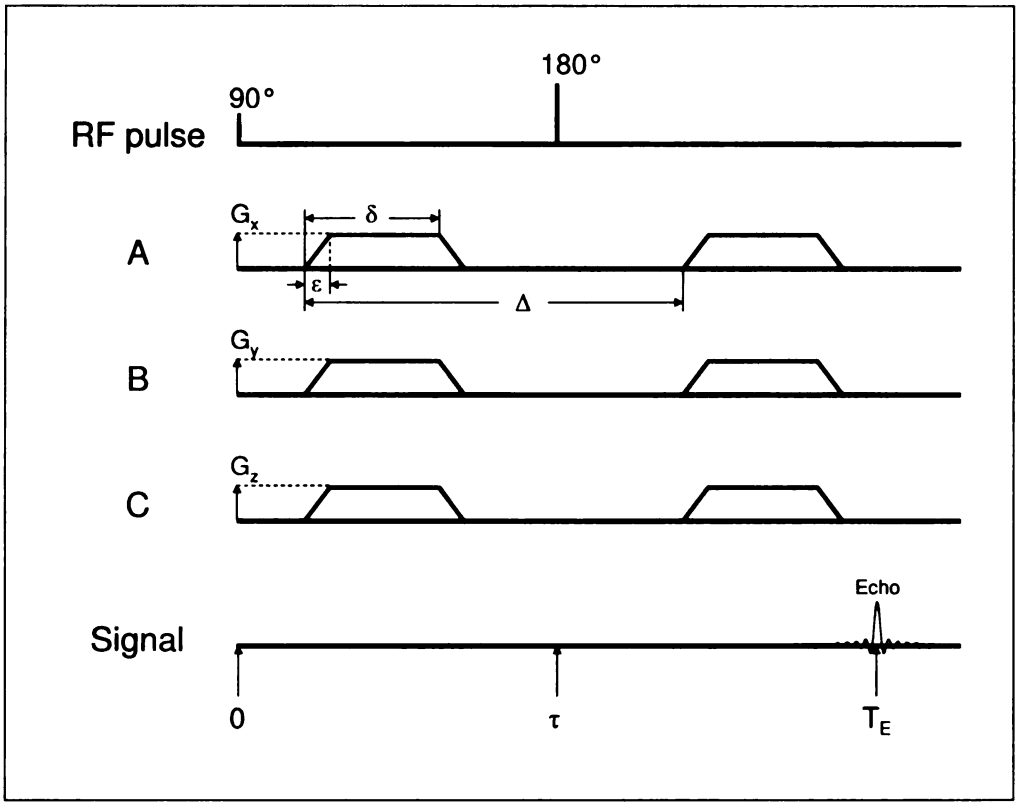

Figure 2.7. Illustrative waveforms for a spin-echo diffusion pulse sequence, defining the parameters ϵ, δ and Δ for (2.8.31). A, B and C denote magnetic field gradients, applied in x-axis (A), y-axis (B) and z-axis (C). Figure adapted from [10].

Chapter 3

Breast lesion analysis tool (BLAT)

3.1 Introduction

BLAT is a software, based on MATLAB (The MathWorks, Natick, MA), that I developed in the course of the project, which is described in this thesis. Its main goal is the automatic detection and analysis of breast lesions. The tool divides into four major tasks:

1. Image reconstruction
2. Lesion boundary detection
3. Surrounding tissue area creation
4. Parameter calculation (discussion see chapters 5 and 6)

3.2 Image processing

3.2.1 Image reconstruction

Patient images are available as binary data with a certain header size on a central server. Given the file name of the patient image of interest, BLAT determines the size of the file and creates a two-dimensional array (i.e., an image) of 512x512 unsigned 16 bit integer

values (DCE case) or 256x256 values (DTI case).

3.2.2 Slice fitting for different image types

DCE images have a different spatial resolution than the DTI images. The slice thickness is 4mm for DTI and 1mm for DCE. The in-plane matrix for DTI is 256x256 and for DCE 512x512. DTI images were expanded to a 512x512 matrix in order to match the DCE matrix. The resolution difference in the direction perpendicular to the image plane is illustrated in Figure 3.1.

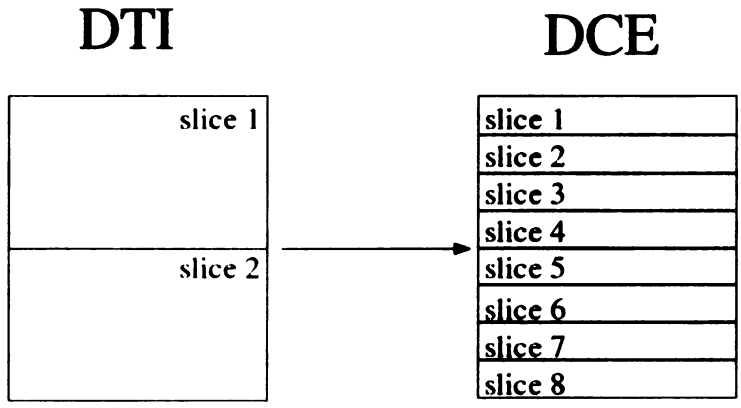

Figure 3.1. Illustration of the different spatial resolution of DTI and DCE images.

The analysis of BLAT described here is based on the evaluation of multiple slices. For the later analysis, the DTI and DCE slices have to match each other: For a specific DTI slice, say "slice 1" in Figure 3.1, DCE "slice 2" was chosen as the corresponding slice, where the DTI image acquisition was centered right between the corresponding DCE slices "slice 2" and "slice 3".

3.2.3 Motion artifact correction

In order to quantify the kinetic behavior of a lesion, it is crucial that there is no shift between the single DCE images corresponding to the same slice. However, due to patient's motion, there might be an image shift in the series that becomes clear by comparing the coordinates of apparent landmarks. A quantitative description of the motion artifacts found in the course of this work can be found in chapter 5. All DCE images were taken in the axial plane - which is the plane in which the midriff lies - with the patient's breast facing downwards, see chapter 4. Although the patients were always asked not to move, a small amount of, for example, breathing-induced movement cannot be eliminated, and will result in a (small) image shift. In order to correct this shift, first a by-eye control should be performed to ensure that there is no image series with apparent shifts in the direction perpendicular to the image plane, which would be more difficult to correct. Landmarks like the nipple can be compared in the image series, and if the landmark doesn't appear (or appears apparently smaller) in some images, an off-image-plane shift is detected and the patient data set should not be included in the study.

BLAT then allows shifting the images by an arbitrary number of pixels in both coordinates of the image plane. A comparison of the position of certain landmarks inside the lesion for images of the DCE series allows reducing motion artifacts in the case of apparent shifts in the axial plane. This shift correction is imperfect, given skewed images as an example. However, cases with such skewed or unclear motion artifacts should not be included in a study using BLAT for the quantitative analysis.

3.2.4 Kinetic feature image creation

After allowing the user to manually correct for possible motion artifacts in the DCE image series, BLAT calculates the wash-in phases for each pixel. For each patient data set, the

wash-in image is calculated as the *relative change* given by the equation

$$I_{rel} = \frac{I_2 - I_1}{I_1}, \tag{3.2.1}$$

where I denotes signal intensity of images and I_i is the i^{th} image in the DCE image time series. I_1 corresponds to the first image of the DCE series, which is the pre-contrast image, and I_2 corresponds to the first phase of the post contrast images.

BLAT also creates images that show the kinetic behavior of the corresponding pixels after the injection of the contrast agent. The DCE image series in this study consist of six images: One pre-contrast (I_1) and five post-contrast images, acquired after fixed time intervals. Each pixel with x- and y-coordinates x, y of a new image 'I_{slope}' is assigned the slope of an interpolated linear function that interpolates the set of dependent values [$I_2(x,y)$, $I_3(x,y)$, $I_4(x,y)$, $I_5(x,y)$, $I_6(x,y)$] to the set of independent values [2, 3, 4, 5, 6] according to the least squares method. Figure 3.2 shows an example of a kinetic curve for a single pixel with the corresponding interpolated function.

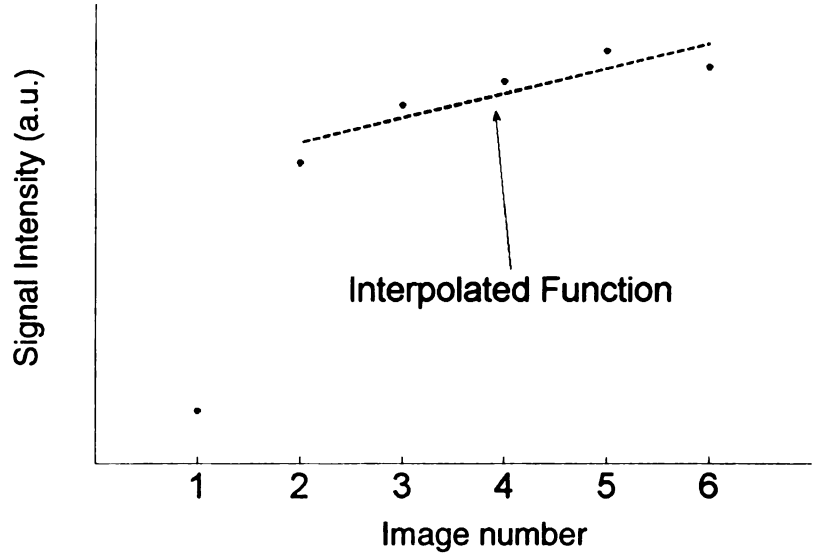

Figure 3.2. An exemplary signal intensity kinetic curve for a single pixel with the corresponding calculated interpolated function.

For a better display leading to the best scattered distribution of slopes for both the lesion

and the surrounding tissue, the slopes are scaled by the factor $1/80$. (Note that the choice of the unit for the abscissa is arbitrary). The slopes are then converted into degree by $\alpha = atan(\text{slope})\frac{180}{\pi}$. An example of an image showing the calculated slopes for the breast lesion that is given in Figure 3.10 in degree for each pixel is shown in Figure 3.3.

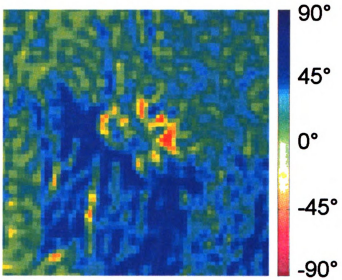

Figure 3.3. The slope image I_{slope} for the breast lesion given in Figure 3.10.

3.3 Lesion boundary detection

The following general criteria have to be considered for the finding of the cut-off threshold for the lesion boundary detection:

1. For different patient subjects the same algorithm with the same parameters has to be used to determine the lesion boundary.
2. Experienced researchers/radiologists have to agree on the detected lesions.
3. The portion of human interference has to be minimized.

The algorithm described below accounts for these criteria. The algorithm was tested on more than 180 different lesions and was found reliable for the detection of lesion margins. For a reliability test, see chapter 5.

3.3.1 The iterative lesion detection algorithm

The user is asked to specify three regions of interest on the image using the mouse:

- an inner boundary of the lesion,
- an outer boundary of the lesion and
- a lesion ROI.

The drawing of an inner and outer bound is included in the software to allow for a manual control of the algorithm. All pixels outside the outer boundary are disregarded and all pixels inside the inner boundary are included in the lesion. This way, the final lesion ROI will be restricted between the outer and the inner boundary. Figure 3.4 shows the individual steps of the algorithm.

After defining the boundaries and the lesion contour, the mean μ and standard deviation σ of the gray-scale values of the pixels inside the lesion area are calculated and a cut-off threshold s of

$$s = \mu - c \cdot \sigma \tag{3.3.2}$$

is calculated. For this study, we chose a cut-off threshold of $\mu - 1.75\sigma$, corresponding to a p-value of $p = 0.04$ (one-tailed t-test).

All values of the pixels between the outer and inner boundary are then compared to s and pixels would be included in the lesion if their values are larger than s. For this new lesion a new cut-off value is calculated according to (3.3.2) and the algorithm is iterated until the lesion reaches a stable area, which would represent the final lesion.

Figure 3.5 shows an example of two differently initially chosen lesion ROIs, the corresponding iteration steps and the final lesion ROIs. The initial selection is hereby marked

green, outer and inner boundary are marked red. The final lesion ROIs differ in eight pixels, which is less than 5% of the lesion area (of the second final lesion).

3.3.2 Test of extreme initial lesion choices

Even for big differences between the initial choices of the lesion ROIs, the algorithm shows a high reliability in delineating the lesion margin: Figure 3.6 shows two different manual initial ROI selections (again the initial selection is marked green and the boundaries are marked red). Figure 3.7 shows the resulting ROIs after the convergence of the algorithm. The first selected area results in an only slightly larger final lesion area. In figure 3.8 all pixels that are counted to the lesion starting with the first initial selection, but not counted to the lesion starting with the second initial selection are set to zero, i.e., they are displayed black. Although there is a large difference between the initially selected areas, the final lesions differ only in relatively few pixels.

3.3.3 Discussion on the choice of the threshold constant c

We analyzed the choice of different threshold values. Figure 3.9 shows the final lesions for the threshold values 1.25, 1.5, 1.75, 2 and 2.25 σ without using inner and outer boundary. As can be seen, the difference between 1.5, 1.75 and 2 σ is not dramatic, however 1.25 and 2.25 σ show dramatically different results. This result supports the choice of $c = 1.75$.

3.3.4 Numerical 1D simulation

We want to consider one line of signal intensity values, that could have been taken from an image of a breast lesion, and apply the iterative algorithm described above to it in order to point out its effectiveness. Table 3.1 shows the iteration steps and corresponding threshold values s for such a one-dimensional example. The center of the lesion shall be the pixel with the value 10, and the initially chosen pixels are the center of the lesion and its two

Iteration	Pixel values of the one-dimensional lesion															s
0 (initial choice)	1	1	2	7	8	9	**9**	**10**	**9**	12	8	7	2	1	1	8.3
1	1	1	2	7	8	**9**	**9**	**10**	**9**	**12**	8	7	2	1	1	7.5
2	1	1	2	7	**8**	**9**	**9**	**10**	**9**	**12**	**8**	7	2	1	1	6.9
3	1	1	2	**7**	**8**	**9**	**9**	**10**	**9**	**12**	**8**	**7**	2	1	1	6.0
4	1	1	2	**7**	**8**	**9**	**9**	**10**	**9**	**12**	**8**	**7**	2	1	1	6.0
Convergence																

Table 3.1. One-dimensional example of the iterational steps of the lesion detection algorithm. The center of the lesion is the pixel with the value 10 and the initially chosen pixels are the center of the lesion and its two neighboring pixels. For each iteration step the pixels that are included in the lesion are written in bold letters. s is the threshold value, corresponding to the specific iteration step.

neighboring pixels. For each iteration step, the pixels that are included in the lesion are written in bold letters. Different initial lesion ROIs may be selected to verify that the algorithm is not highly sensitive to the initial selection.

Convergence discussion

Generally, the algorithm lets the lesion expand until it finds a relatively large step between the intensity values of two neighboring pixels, i.e., the difference between these two values has to be large enough so that the threshold values s' and s'' of two subsequent iterations both lie in the interval between the two pixel values. The lesion will continue to increase from iteration step to step if there is no clear jump of the pixel values at the lesion margin. In such cases, where it is also by eye hard or impossible to tell where the lesion ends, the outer boundary comes into play, and we draw it in such a way that we exclude those parts outside the lesion, within which we are sure that they do not belong.

3.4 Tissue area creation

After having found the lesion area, a layer of one pixel width is created as a 'gap' between the lesion area and the tissue areas to be created. The gap accounts for the *partial volume effect*, which has to be taken into account when voxels are covering different areas of interest. Following pixel layers are added to the lesion until the new area, which we want to call *tissue 1*, has the same area of the original lesion[1].

Layers are added by including all pixels in the 8-connected neighborhood of the margin pixels to the last layer. The same way, a second tissue area called *tissue 2* is also created, directly surrounding *tissue 1*.

Figure 3.10 shows an example for a detected lesion with the surrounding tissue areas. Hereby, the inner black contour denotes the one pixel wide gap between the lesion and the tissue 1 area; the middle contour denotes the last pixel layer of the tissue 1 area and the same way the outer contour denotes the last pixel layer of the tissue 2 area.

[1] By adding whole pixel layers at one time, the wanted area is in most cases not exactly obtained. Therefore the algorithm adds layers until the absolute value of the difference between the lesion area and the tissue 1 area is minimized and then pixels of the margin are taken away or pixels are added at the layer directly surrounding the margin, respectively, until the areas equal each other.

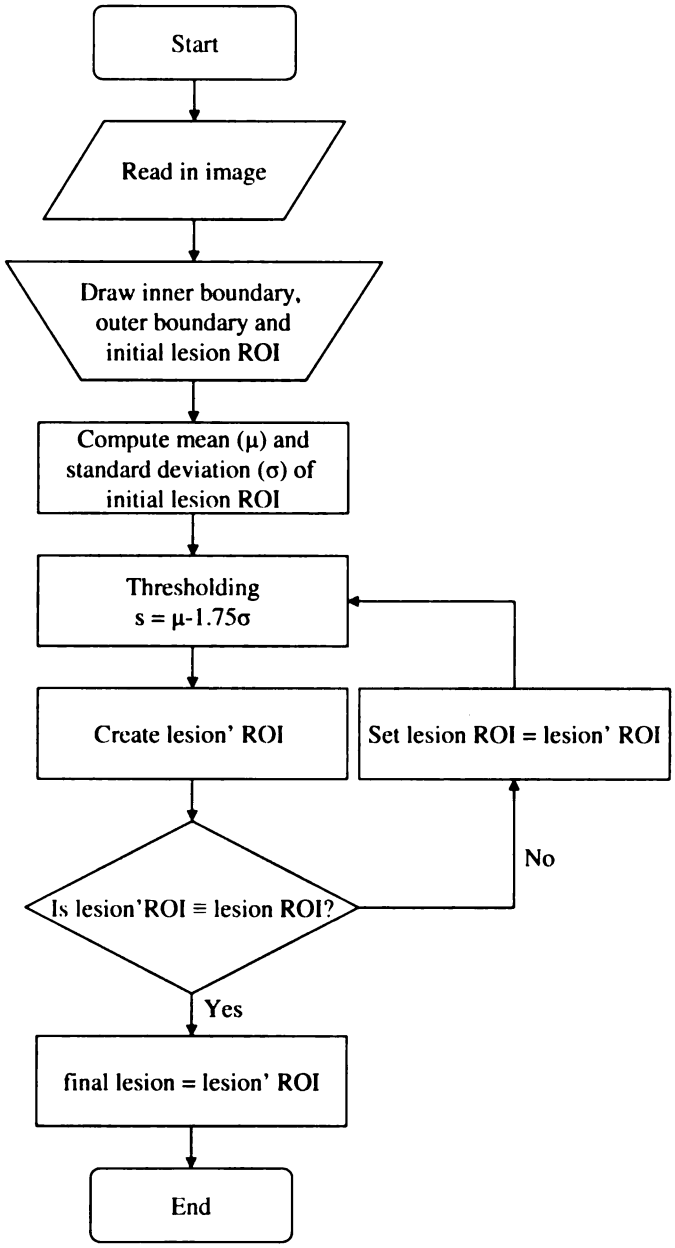

Figure 3.4. The iterative lesion boundary detection algorithm: The threshold value s is calculated on the basis of the mean μ and the standard deviation σ of the before defined lesion ROI. All pixels with values larger than s are assembled to make up the lesion' ROI.

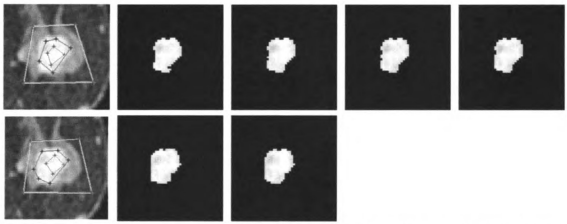

Figure 3.5. Two differently chosen initial lesion ROIs and the corresponding iteration steps of the boundary detection algorithm. The initial chosen lesion ROI is marked green and the two boundaries are marked red. The algorithm for the first initial chosen ROI (first line) converges after four iterations and the last ROI in the first line is the corresponding final ROI. For the second initial chosen ROI the algorithm converges after only two iterations.

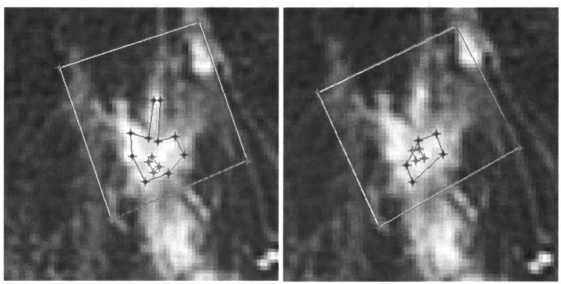

Figure 3.6. Two possible initial ROI selections. Left: choice 1. Right: choice 2. The manually selected lesion area is displayed green, inner and outer boundaries are displayed red.

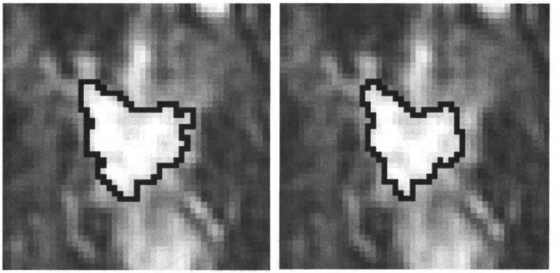

Figure 3.7. Final lesion area after convergence of the algorithm for the initially selected areas shown in Figure 3.6. Left: choice 1. Right: choice 2.

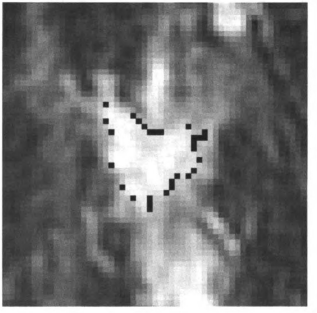

Figure 3.8. Difference image, showing all pixels that differ between the final lesions in Figure 3.7 in black.

Figure 3.9. Final lesion ROIs for differently chosen cut-off values. From left to right: $c = 1.25, 1.5, 1.75, 2, 2.25$.

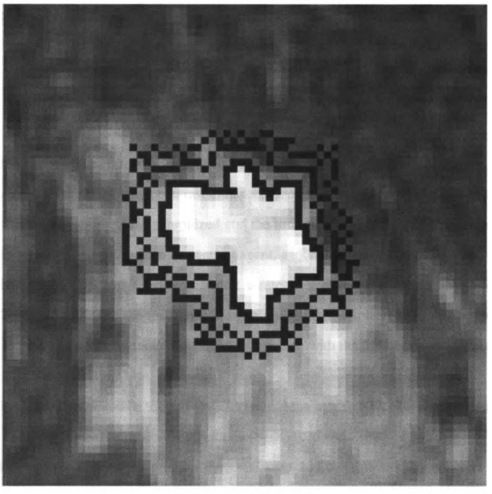

Figure 3.10. An example for a detected lesion and its surrounding tissue areas. The inner black contour denotes the one pixel wide gap between the lesion and the tissue 1 area; the middle contour denotes the last pixel layer of the tissue 1 area and the same way the outer contour denotes the last pixel layer of the tissue 2 area.

Chapter 4

Methods and Materials

4.1 MRI

Imaging was performed at a GE 1.5 T clinical scanner (General Electric HealthCare, Milwaukee, WI). For the dynamic contrast-enhanced imaging, the contrast agent injection and the dynamic imaging were synchronized and the time interval between two post-contrast images was set to 90 seconds. As a contrast agent, gadobenate dimeglumine (Gd-BOPTA, 0.2mL/kg) was used and it was injected at a rate of 3cc/s over 7-10 seconds followed by a 20-cc saline flush. For the dynamic imaging in the axial plane a 3D fat-suppressed T1-weighted fast spoiled-gradient-echo pulse sequence with the following parameters was used:

TE/TR=2.8/5.9 ms, Field of View (FOV) 320 mm, Matrix 320x320, Flip Angle (FA) 10°, Slice thickness 2 mm, Number of Excitations (NEX) 0.76 and ZIP2.

The DTI scan was acquired prior to the DCE scan and the following parameters were used: FOV 320 mm, TE/TR=min/10000ms, matrix 160x160, slice thickness 4mm, gap 0mm, NEX 2, b = $600s/mm^2$. Diffusion encoding was accomplished in six non-collinear directions.

4.2 Image Data

Anonymous breast MRI data was examined. Sixteen contrast-enhanced lesions were included in this study. Among these, ten were grouped as malignant and six as benign, according to the pathology reports. The malignant tumors included infiltrating invasive ductal carcinomas, grades I-III, and the benign lesions fibroadenomas and fibrocystic changes. The DCE analysis was based on all 16 masses. For the DTI analysis one malignant case with a large apparent necrotic area was omitted, since the mean diffusivity and fractional anisotropy of necrotic areas are awaited to significantly change for necrotic areas.

4.2.1 Discussion of a possibly false negative biopsy result ($\triangle$)

It is highly probable that one out of the six examined benign cases was truly malignant. After the MR scan, two subsequent biopsies were performed for this subject and both times the diagnosis was negative for atypia or malignancy, categorizing the lesion as fibrocystic. However, a mastectomy with a subsequent examination of the breast was carried out three months after the last biopsy, finding the whole breast to be exceedingly interspersed with malignant substance. A malignant lesion (infiltrating ductal carcinoma) was found, which according to the mastectomy report most probably corresponded to the lesion analyzed at the two prior biopsies, revealing most probably false negative biopsy results. In this work, this case has been assigned to the benign group, according to our inclusion criterion of a negative pathology report. It is however marked in all relevant figures with the special symbol $\triangle$.

Chapter 5

Dynamic Contrast-Enhanced Imaging Data Analysis

5.1 DCE motion artifacts

The mean absolute value of the shift in anterior/posterior direction was found to be 0.55 pixels with a shift maximum of 3 pixels. The mean absolute value of the left/right shift was found to be 0.25 pixels with a shift maximum of 2 pixels. There was no off-image-plane shift found.

5.2 ROI test

A statistical analysis, based on the DCE images, was performed in order to validate that the algorithm described in chapter 3.3.1 truly picks up the lesion and separates lesion and tissue into two groups of significant difference. For the lesions, the signal intensity's mean and standard deviation were calculated to 1582 ± 334; for the tissue 1 area, to 673 ± 161; and for the tissue 2 area, to 583 ± 142, revealing a significant difference between the lesion and the tissue 1 area with $p < 10^{-7}$ (students' t-test), but no significant difference was detected between the two tissue areas ($p > 0.10$), which was the awaited result.

In a second step, the uptake signal changes r_{12} for the lesion and the tissue 1 and tissue 2 areas were calculated and compared. r_{12} is given by the mean relative change value reflected in the wash-in image, which has been discussed in chapter 3.2.4. The uptake signal change for the benign lesions was $(111 \pm 39)\%$, for their surrounding tissues $(50 \pm 20)\%$, for the malignant tumors $(140 \pm 33)\%$ and for their surrounding tissues $(62 \pm 27)\%$. For both the benign and the malignant case the difference between lesion and tissue area was significant ($p < 0.009$ and $p < 10^{-4}$, respectively). There was however no significant difference between the benign lesions and the malignant tumors ($p > 0.16$). This result is consistent with the radiologic reports of suspicion for malignancy, taking into account that it has been reported that most invasive breast cancers show fast strong enhancement and that benign lesions tend to have lower enhancement rates than the malignant ones [14].

5.3 Kinetic behavior analysis

Mean relative change kinetic curves for the benign lesions, the malignant tumors and the tissue areas are plotted in Figure 5.1. Note the clearly distinct kinetic behaviors of the lesions and the tissue areas in Figure 5.1, which furthermore supports the boundary determination using the presented algorithm. Also, the benign lesions show a slightly different kinetic behavior than the malignant lesions: the mean uptake rate for the benign lesions is lower than that for the malignant tumors - however, insignificantly lower, as shown above - and the kinetic behavior from the first to the last post-contrast enhanced image shows a persistent behavior for the benign cases in contrast to a plateau or slight wash-out behavior for the malignant cases. The mean slope m, given as the mean of the pixel values in I_{slope} (see chapter 3.2.4) of the lesion areas, was calculated for the benign ($m = (30.2 \pm 10.2)°$) and the malignant case ($m = (2.1 \pm 12.6)°$). The difference is significant ($p \simeq 3.9 \cdot 10^{-4}$), which demonstrates the potential of the mean slope value of the detected lesions for the delineation between malignant and benign lesions. Figure 5.2 shows the slope distribution

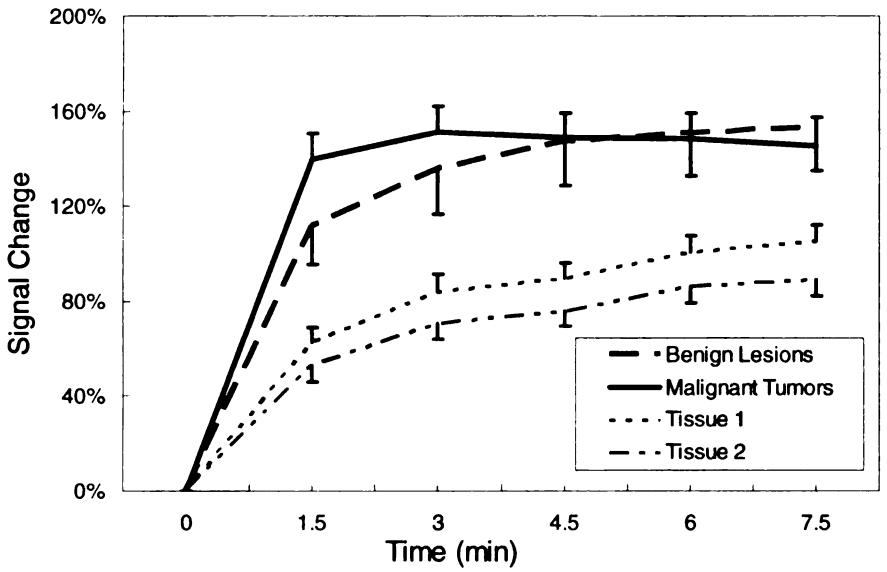

Figure 5.1. Mean relative change kinetic curves for benign lesions and malignant tumors and their surrounding tissue areas. The error bars denote the standard error of means.

for the malignant and the benign cases.

5.4 Combining kinetic information to delineate between malignant tumors and benign lesions

We introduced a method to combine the kinetic information between the pre-contrast and the first post contrast-enhanced image, i.e., data given by the wash-in image, and between the first and the last post contrast-enhanced image, i.e., data given by I_{slope}. It is commonly accepted that both phases can be used for the delineation between malignant and benign masses, see e.g. [5, 15]. However, to our knowledge no attempt has been made to date to (1) combine both phases for a (2) quantitative analysis using (3) the automatically detected whole lesion ROI instead of the most enhancing area. We show that for our sample a clear separation between the benign and the malignant group was yielded, using our method ($p < 3 \cdot 10^{-4}$).

We calculated *slope wash-in* images in conformance with the slope images I_{slope}, see 3.2.4.

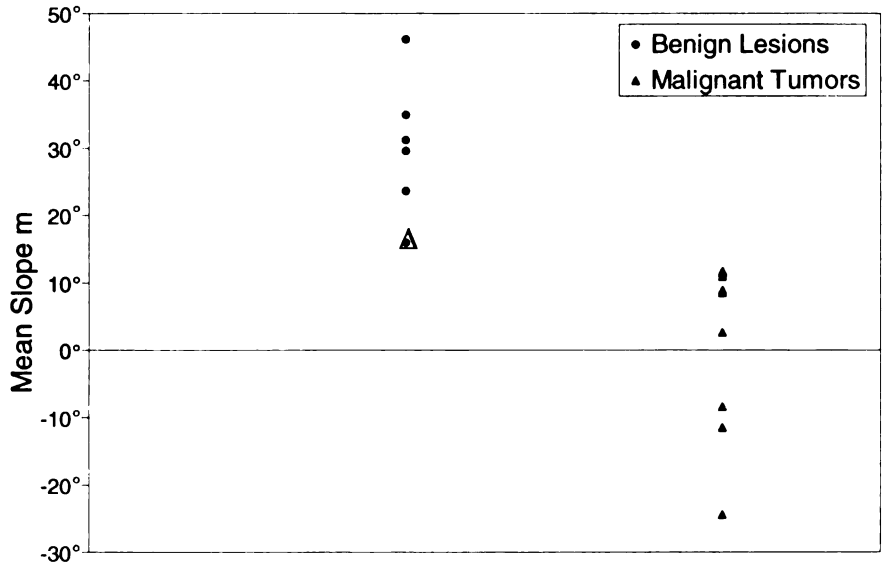

Figure 5.2. The distribution of the mean slopes of the kinetic behavior of the detected lesions after the first post contrast-enhanced image. △ denotes the possibly false negative case.

	Ξ
malignant	$(97.9 \pm 13.4)°$
benign	$(129.6 \pm 11.2)°$
p-value	$2.7 \cdot 10^{-4}$

Table 5.1. Mean and standard deviation of the slope-angle Ξ for benign and malignant masses with corresponding p-value.

The correlation coefficient between the mean slopes from I_{slope} and the mean wash-in slopes was $R^2 = 0.31$ with $p < 0.02$. A strong uptake rate was therefore correlated with a strong wash-out, which allowed us to combine the information given by both phases. The angle Ξ between the slope wash-in image and I_{slope} was calculated and we awaited a lower Ξ for malignant tumors than for benign lesions. Figure 5.3 defines Ξ. The calculation of Ξ yielded the results given in table 5.1.

The distribution of Ξ is plotted in Figure 5.4.

Considering the clear separation of the benign and the malignant group, we conclude that

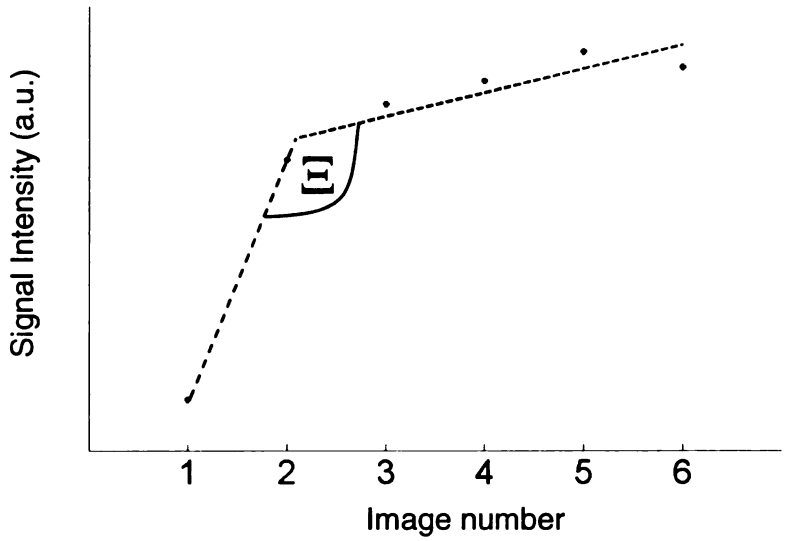

Figure 5.3. The slope angle Ξ between the wash-in slope function and the interpolated slope-function between the first and last post contrast-enhanced image for an exemplary kinetic curve.

the mean slope angle clearly provides clinical potential for the delineation of malignant and benign lesions.

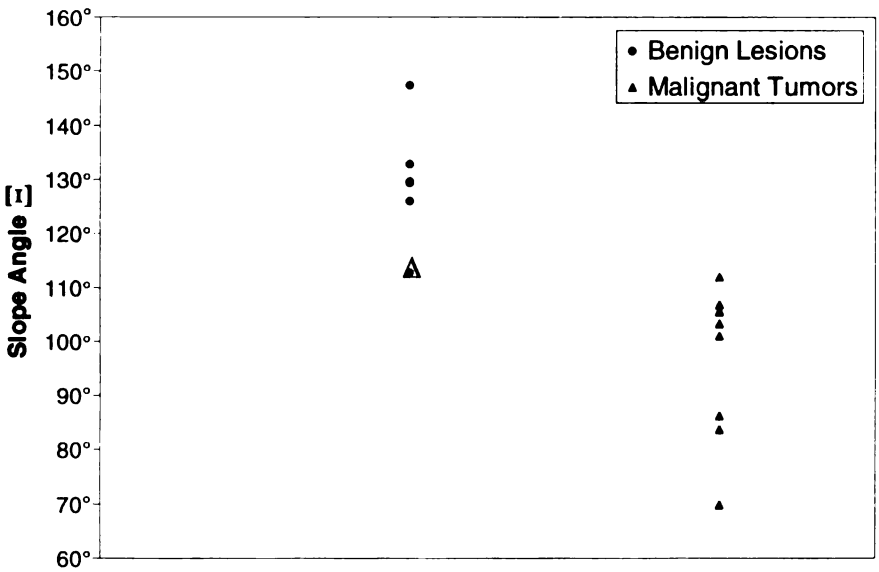

Figure 5.4. The distribution of the slope angle Ξ. △ denotes the possibly false negative case.

Chapter 6

Diffusion Tensor Imaging Data Analysis

So far, we used DCE imaging to improve the characterization of breast lesions. The physiological reasoning for the comparison of kinetic features is hereby the increased vascularity of malignant tumors (see chapter 2.7). DCE imaging, however, does not reveal direct information about lesion *cellularity* (cell density), which has also been shown to be an important index of tumor grade [4]. In particular, malignant tumors are known to be hypercellular in comparison to benign lesions [4].

Brownian motion of water molecules in a tissue is affected by the microscopic structure of the tissue. A high cell density if therefore expected to reduce the water diffusion because of the high restriction to the diffusion. It has indeed been observed that the lesion mean diffusivity correlates with tumor cellularity [6], revealing the potential of the mean diffusivity for a delineation between malignant tumors and benign lesions according to their different cellularities [6, 23, 16]. However, these studies also revealed that there was a large overlap between the mean diffusivity values of benign and malignant masses. A recent preliminary study introduced a method of using relative mean diffusivity changes to establish a statistical model for quantitatively characterizing breast lesions [9].

In this study, we first examined the mean diffusivity for both the lesions and their surrounding tissues, and a large variation in diffusivity was observed among the subjects. The

large tissue variation in mean diffusivity from subject to subject is likely to be a cause for the large overlap between the benign and the malignant group. To examine this possibility, we also investigated the correlation between the mean diffusivity of the lesion and the surrounding tissue, and a correlation was found. This correlation provides a reason for introducing the relative mean diffusivity change that accounts for the variation from subject to subject.

Subsequently, using the relative mean diffusivity change, we found a significant separation of the benign and malignant groups ($p > 0.006$) in contrast to no significant difference comparing the mean diffusivity ($p > 0.23$). We also examined the fractional anisotropy and relative fractional anisotropy of the benign and malignant cases.

6.1 DTI motion artifacts

BLAT allows for the manual correction of shift artifacts between the DCE and DTI images in the same way as discussed above for the DCE image series. The mean absolute value of the shift in anterior/posterior direction was found to be 1.60 pixels with a shift maximum of 6 pixels. The mean absolute value of the left/right shift was found to be 4.00 pixels with a shift maximum of 11 pixels. There was no off-image-plane shift found.

6.2 Mean diffusivity calculations

The created lesion, tissue 1 and tissue 2 ROIs (see chapter 3.3) were applied to the DTI images to both calculate the mean diffusivity and, later, the fractional anisotropy for the lesion and tissue ROIs. The results are given in Table 6.1. The data show that there is a large tissue variation between subjects, which is awaited and consistent with the common practice to group tissue into four different types: almost entirely fat, scattered fibroglandular densities, heterogeneously dense and extremely dense [1]. The difference between the mean diffusivity of the malignant lesions and their surrounding tissue 1 area is significant

($p \simeq 0.0069$); however, the difference between the mean diffusivity of the two tissue areas is not significant ($p \simeq 0.83$). The difference between the mean diffusivity of the benign lesions and their surrounding tissue is not significant ($p \simeq 0.66$ between lesion and tissue 1, $p \simeq 0.70$ between tissue 1 and tissue 2). Since lesion cellularity has been shown to correlate with lesion mean diffusivity [6], we considered that benign lesions might have a similar cellularity as normal tissue.

The distribution of the mean diffusivity is plotted in Figure 6.1, which shows a huge overlap between the malignant and the benign group. No significant difference between the two groups is found ($p > 0.23$). Therefore, comparing the mean diffusivity was for our sample

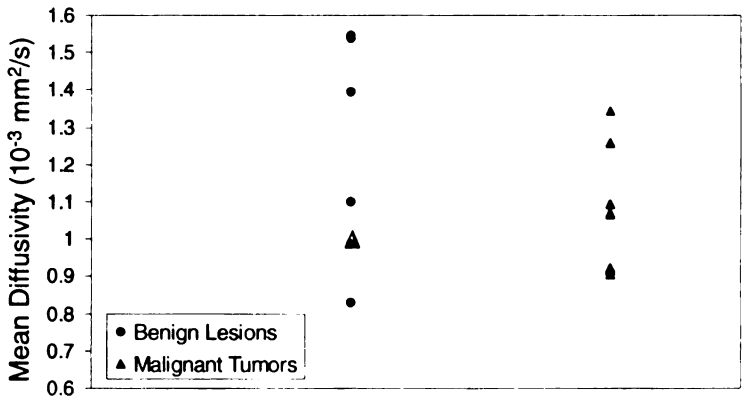

Figure 6.1. Mean diffusivity distribution for malignant tumors and benign lesions. △ denotes the possibly false negative case.

not a reliable method to characterize breast lesions.

6.3 Fractional anisotropy calculations

The fractional anisotropy was calculated for the lesion and tissue areas for both benign and malignant cases. The results are shown in Table 6.1. Again the data show that there is a large tissue variation between subjects. The difference between the fractional anisotropy

	$\langle D \rangle$ $(10^{-3} mm^2/s)$		FA	
	Malignant Tumors	Benign Lesions	Malignant Tumors	Benign Lesions
Lesion	1.05 ± 0.16	1.23 ± 0.30	0.43 ± 0.08	0.46 ± 0.13
Tissue 1	1.32 ± 0.20	1.17 ± 0.20	0.55 ± 0.10	0.62 ± 0.12
Tissue 2	1.35 ± 0.23	1.12 ± 0.19	0.58 ± 0.12	0.67 ± 0.14

Table 6.1. Mean diffusivity $\langle D \rangle$ and fractional anisotropy FA for malignant tumors, benign lesions and their surrounding tissue areas ($\mu \pm \sigma$).

of the malignant lesions and their surrounding tissue 1 area is significant ($p \simeq 0.01$); however, the difference between the fractional anisotropy of the two tissue areas is again not significant ($p \simeq 0.58$). For the benign case we get a significant difference comparing the tissue 1 and the lesion area ($p \simeq 0.04$) and not a significant difference for the tissue area comparison ($p \simeq 0.56$).

The fractional anisotropy distribution is plotted in Figure 6.2. There is no significant difference between the malignant and the benign masses ($p > 0.66$). Therefore, the fractional

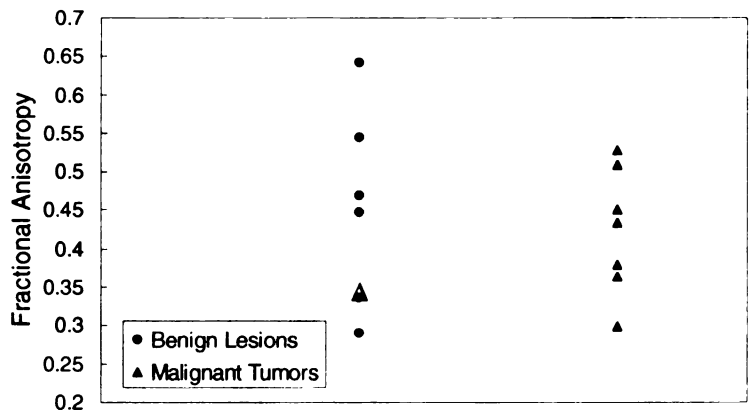

Figure 6.2. Fractional anisotropy distribution for malignant tumors and benign lesions. △ denotes the possibly false negative case.

anisotropy is also not sensitive enough to delineate between malignant tumors and (suspicious) benign lesions for our sample.

6.4 Statistical justification for the introduction of the relative change concept

6.4.1 Lesion-tissue correlation analysis

In order to quantify the possible dependence between the tissue and the lesion properties, we drew scatter plots with linear trend lines of the lesion and tissue 1 mean diffusivity and fractional anisotropy, respectively (see Figures 6.3 and 6.4). The equations for the linear trend lines are given in the figures. For the mean diffusivity, the correlation coefficient R^2 was calculated to $R^2_{\langle D \rangle} = 0.21$ with $p < 0.09$ and for the fractional anisotropy we got $R^2_{FA} = 0.44$ with $p < 0.01$. The fractional anisotropy shows a significant correlation between the tissue and the lesion area. This correlation may be used to possibly reduce the large variation from subject to subject. Using the common significance level of 5%, there is no significant correlation between the lesion and tissue mean diffusivity. However, since the p-value is not much bigger than the commonly accepted significance level threshold value, we still assumed a linear dependency. Additional studies with larger samples are needed to examine further the correlation between lesion and tissue mean diffusivity.

6.4.2 Tissue-tissue correlation analysis

We analyzed the correlation between tissue 1 and tissue 2. Figure 6.5 and 6.6 show the linear correlation between tissue 1 and tissue 2 areas for both the mean diffusivity ($p < 7 \cdot 10^{-7}$) and fractional anisotropy ($p < 2 \cdot 10^{-7}$). From the trend line equations given in both figures it becomes clear that the two tissue areas show always about the same behavior. Accordingly, either the tissue 1 area or the tissue 2 area could be taken as a reference that most probably reflects the mean normal breast tissue values of $\langle D \rangle$ and FA, respectively, of the specific subject. For this study, we chose the tissue 1 area as a reference.

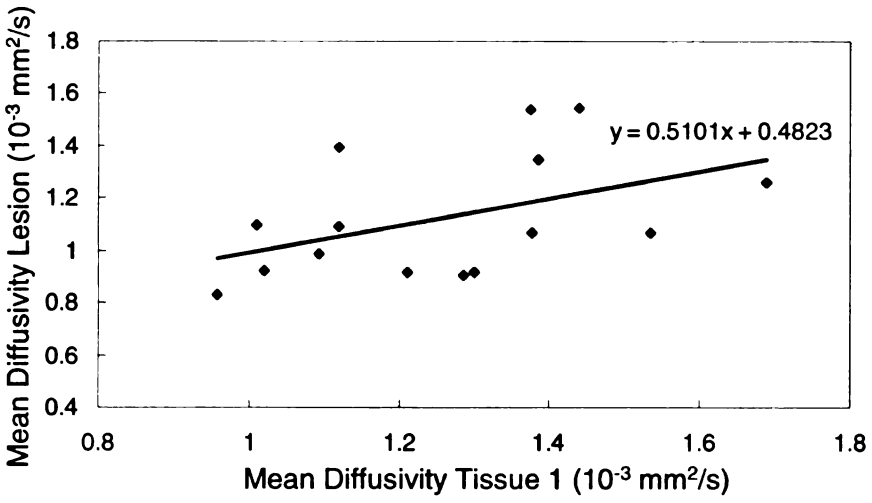

Figure 6.3. Mean diffusivity correlation between tissue 1 and lesion area.

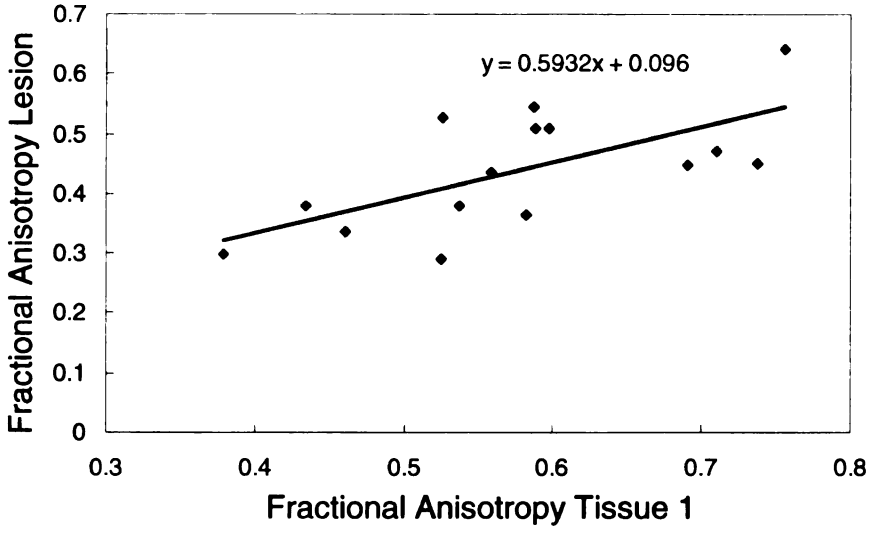

Figure 6.4. Fractional anisotropy correlation between tissue 1 and lesion area.

6.5 Introduction of the mean diffusivity relative change model and results

We introduce the relative change X_r as

$$X_r = \frac{X_l - X_t}{X_t}, \tag{6.5.1}$$

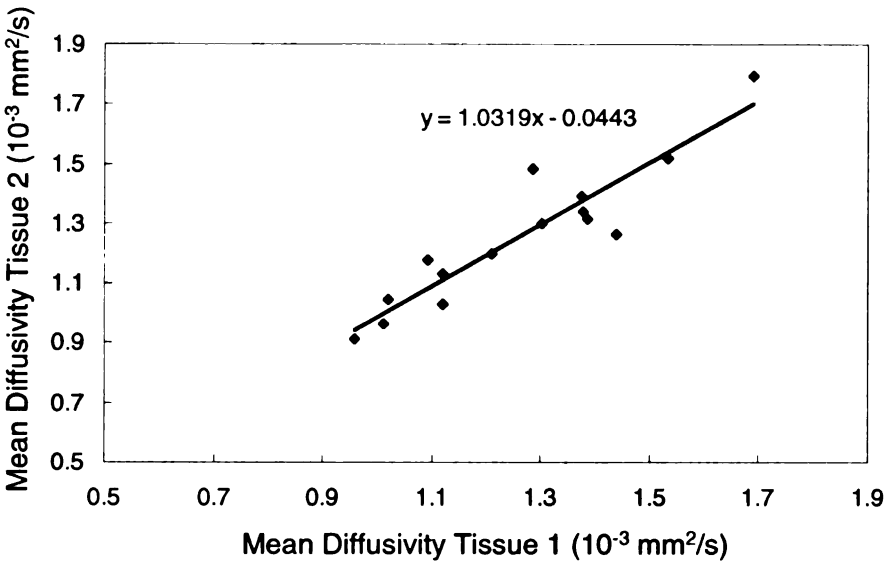

Figure 6.5. Mean diffusivity correlation between tissue 1 and tissue 2 area.

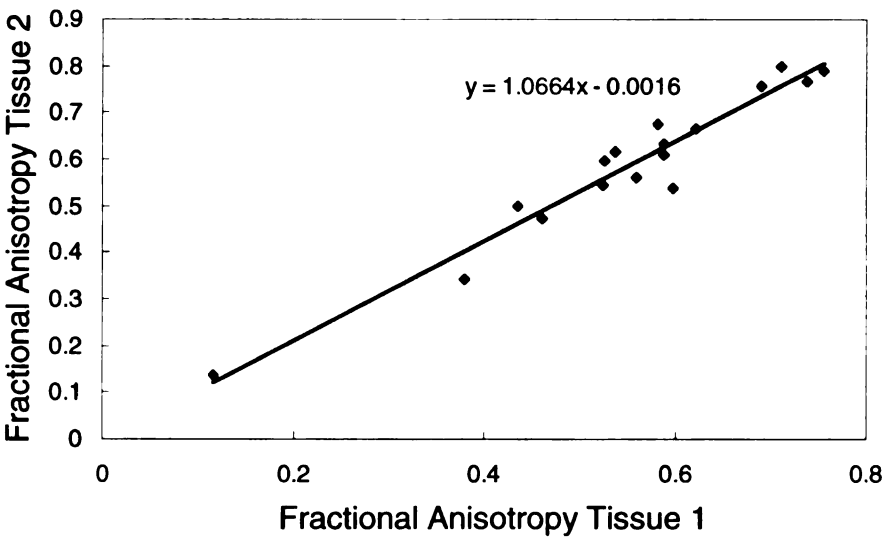

Figure 6.6. Fractional anisotropy correlation between tissue 1 and tissue 2 area.

where X denotes a quantity such as the mean diffusivity or the fractional anisotropy and the index l denotes the lesion area and t the tissue 1 area.

Figure 6.7 shows the distribution of the relative mean diffusivity values of the lesions. Their corresponding means, standard deviations and p-value are given in Table 6.2. As can be seen, the introduction of the relative mean diffusivity change significantly separates the

	$\langle D \rangle_r$	FA_r
malignant	-0.197 ± 0.114	-0.211 ± 0.068
benign	0.049 ± 0.141	-0.272 ± 0.126
p-values	0.006	0.41

Table 6.2. Relative mean diffusivity and relative fractional anisotropy ($\mu \pm \sigma$) for benign and malignant cases.

malignant distribution from the benign distribution, thus revealing clinical potential for the delineation of benign and malignant masses. However, there is still an overlap between the groups.

The relative mean diffusivity of the benign lesions is distributed around the tissue values (i.e., around zero), as awaited, since the benign lesions show similar behavior as their surrounding tissue (see discussion above).

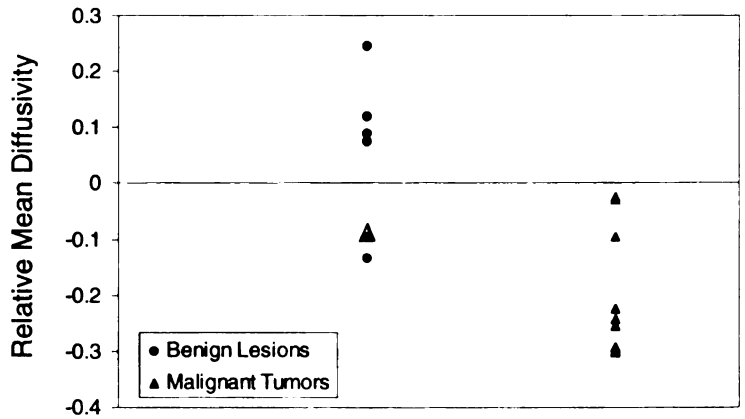

Figure 6.7. Relative mean diffusivity distribution for malignant tumors and benign lesions. △ denotes the possibly false negative case.

Figure 6.8 shows the distribution of the relative fractional anisotropy change values, FA_r. Their corresponding means, standard deviations and p-value are also given in Table 6.2. Fractional anisotropy and relative fractional anisotropy seem to be not sensitive enough for a reliable delineation between malignant and benign masses.

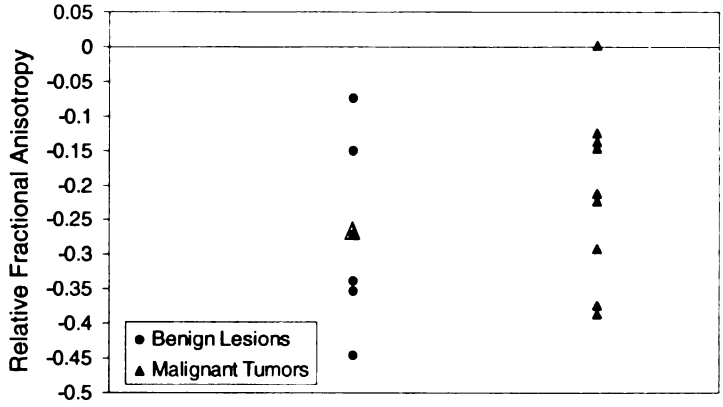

Figure 6.8. Relative fractional anisotropy distribution for malignant tumors and benign lesions. △ denotes the possibly false negative case.

6.5.1 Detailed DTI subject data

The individual subject DTI data is given in Table 6.3.

Figure 6.9 shows the normalized mean diffusivity distribution for all malignant (A) and benign (C) lesions and the normalized relative mean diffusivity distribution for malignant (B) and benign (D) lesions. We set up a statistical model for the malignant tumors, given the mean and standard deviation of the relative mean diffusivity distribution. The corresponding Gaussian distribution is plotted in Figure 6.9(B). Means and standard deviations for the four distributions in Figure 6.9 are given in Table 6.4. The standard deviation of the mean diffusivity distributions is larger than that of the relative mean diffusivity distribution, which supports the assumption that the normal tissue mean diffusivity biases the mean diffusivity distribution and that the introduction of the relative change corrects for this distortion.

	$\langle D_l \rangle$	$\langle D_{t1} \rangle$	$\langle D_{t2} \rangle$	$\langle D \rangle_r$	FA_l	FA_{t1}	FA_{t2}	FA_r
1	1.395	1.031	1.031	0.245	0.447	0.690	0.758	−0.353
2	0.830	0.958	0.911	−0.134	0.642	0.756	0.790	−0.150
3	1.099	1.010	0.963	0.088	0.470	0.710	0.799	−0.338
4	1.538	1.375	1.390	0.118	0.291	0.525	0.544	−0.446
5	1.547	1.439	1.264	0.075	0.544	0.588	0.633	−0.074
6 △	0.987	1.093	1.177	−0.097	0.336	0.461	0.472	−0.271
7	0.904	1.286	1.483	−0.297	0.298	0.379	0.343	−0.213
8	1.257	1.689	1.793	−0.256	0.508	0.589	0.610	−0.137
9	0.915	1.211	1.200	−0.244	0.380	0.537	0.616	−0.292
10	0.923	1.021	1.046	−0.096	0.364	0.582	0.676	−0.374
11	1.069	1.534	1.520	−0.303	0.509	0.598	0.537	−0.148
12	1.092	1.119	1.131	−0.025	0.452	0.737	0.767	−0.388
13	1.067	1.378	1.338	−0.225	0.527	0.526	0.598	0.001
14	1.344	1.385	1.314	−0.030	0.380	0.434	0.499	−0.126
15	0.920	1.301	1.299	−0.293	0.435	0.559	0.560	−0.222

Table 6.3. Data of the DTI image analysis with benign cases (1-6) and malignant cases (7-15) for lesion (l), tissue 1 ($t1$) and tissue 2 ($t2$) areas. Mean diffusivity values are given in $10^{-3}mm^2/s$. △ denotes the possibly false negative case.

	$\langle D \rangle$ $(10^{-3}mm^2/s)$	$\langle D \rangle_r$
malignant	1.11 ± 0.33	-0.15 ± 0.25
benign	1.22 ± 0.41	0.03 ± 0.28

Table 6.4. Mean diffusivity $\langle D \rangle$ and relative mean diffusivity $\langle D \rangle_r$ ($\mu \pm \sigma$) of the distributions given in Figure 6.9.

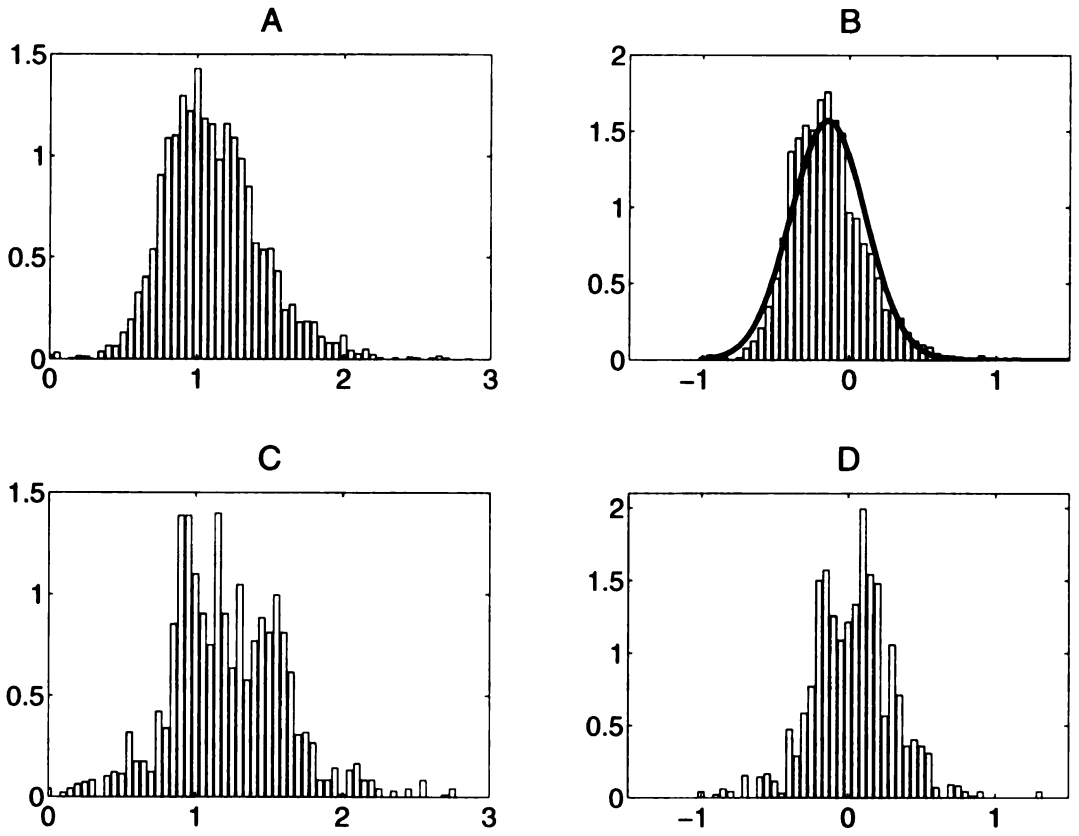

Figure 6.9. Normalized mean diffusivity for malignant tumors (A) and benign lesions (C) and normalized relative mean diffusivity distribution for malignant tumors (B) and benign lesions (D). In (B) the Gaussian distribution according to the set up statistical model is included.

Chapter 7

Discussion

The breast lesion analysis software that was created in the course of this work was validated, and it presented a reliable method to identify lesions. A method using combined kinetic informations was introduced and it revealed potential for later clinical applications for the delineation between malignant and benign breast masses.

The recently evolving diffusion tensor imaging technique was used and examined for usability for the characterization of breast lesions. So far, it seems to bear less potential for a reliable delineation criterion than dynamic contrast-enhanced imaging. However, a statistical justification for the introduction of the relative change concept was found, and the relative mean diffusivity change was demonstrated to significantly improve the separation of the benign and malignant group in comparison to the approach using the mean diffusivity. Further studies have to be done in order to evaluate the clinical usability of DTI for the characterization of breast lesions, in particular with regard to the fractional anisotropy.

APPENDICES

Appendix A

Gyromagnetic ratios

$\gamma/2\pi$	(MHz/T)
^{1}H (proton)	42.576
electron	28024.954
neutron	29.165
^{7}Li	16.546
^{13}C	10.705
^{14}N	3.0766
^{15}N	-4.3156
^{17}O	-5.7716
^{23}Na	11.262
^{31}P	17.235

(Values for electron and neutron from [17]. All other values from [2]).

Bibliography

Bibliography

[1] LW Bassett and CH Kim. Breast imaging: Mammography and ultrasonography. *MRI Clinics of North America*, 9:251–271, 2001.

[2] MA Bernstein, KF King, and XJ Zhou. *Handbook of MRI Pulse Sequences*. Elsevier Academic Press, 2004.

[3] J Crank. *The mathematics of diffusion*. Oxford University Press, New York, 1993.

[4] BS Ducatman, ST Emery, and HH Wang. Correlation of histologic grade of breast carcinoma with cytologic features on fine-needle aspiration of the breast. *Mod Pathol*, 6:539–543, 1993.

[5] IS Gribbestad, G Nilsen, HD Fjøsne, S Kvinnsland, OA Haugen, and PA Rinck. Comparative signal intensity measurements in dynamic gadolinium-enhanced mr mammography. *J Magn Reson Imaging*, 4(3):477–480, 1994.

[6] Y Guo and Y Cai et al. Differentiation of clinically benign and malignant breast lesions using diffusion-weighted imaging. *J Magn Reson Imaging*, 26:172–178, 2002.

[7] EM Haacke, RW Brown, MR Thompson, and R Venkatesan. *Magnetic Resonance Imaging: Physical Principles and Sequence Design*. John Wiley and Sons, 1999.

[8] J Hrung, S Sonnad, J Schwartz, and C Langlotz. Accuracy of mr imaging in the work-up of suspicious breast lesions: a diagnostic meta-analysis. *Acad Radiol 6*, 7:387–397, 1999.

[9] J Huang, L Hoisington, A Babayan, and K Berger. Differentiation of malignant from benign breast lesions using relative adc changes. Not yet published.

[10] J Huang and DC Zhu. Simultaneous magnetic resonance imaging of diffusion anisotropy and diffusion gradient. *J Magn Reson Imaging*, 26:337–346, 2008.

[11] TS Ibrahim. Analytical approach to the mr signal. *Magnetic Resonance In Medicine*, 54 (3):677–682, 2005.

[12] L Jeremy. Breast cancer cases rise 80% since secenties. *The Independent*, 2006.

[13] CK Kuhl. *Dynamic Breast Magnetic Resonance Imaging*, chapter 7. Springer, 2005.

[14] CK Kuhl. Concepts for differential diagnosis in breast mr imaging. *Magn Reson Imaging Clin N Am*, 14:305–328, 2006.

[15] CK Kuhl and P Mielcareck et al. Dynamic breast mr imaging: Are signal intensity time course data useful for differential diagnosis of enhancing lesions? *Radiology*, 211(1):101–110, 1999.

[16] Y Kuroki, K Nasu, S Kuroki, K Murakami, T Hayashi, R Skiguchi, and S Nawano. Diffusion-weighted imaging of breast cancer with the sensitivity encoding technique: Analysis of the apparent diffusion coefficient. *Magnetic Resonance In Medicine*, 3:79–85, 2004.

[17] National Institute of Standards and Technology. http://www.nist.gov.

[18] L Onsager. Reciprocal relations in irreversible processes. i. *Phys. Rev.*, 37:405–426, 1931.

[19] L Onsager. Reciprocal relations in irreversible processes. ii. *Phys. Rev.*, 38:2265–2279, 1931.

[20] World Health Organization. World cancer report. retrieved 02/03/2008.

[21] SC Partridge, PW Richardson, JM Lorenzo, S Peacock, WB DeMartini, PR Eby, EL Rosen, and CD Lehman. Discrimination of benign and malignant breast lesions by diffusion tensor mri. In *Screening: New Imaging Modalities*. American Society of Clinical Oncology, 2007.

[22] MD Schnall. An overview of interpretation strategies for breast mr imaging. *MRI Clinics of North America*, 9:289–293, 2001.

[23] S Sinha, FA Lucas-Quesada, U Sinha, N DeBruhl, and LW Bassett. In vivo diffusion-weighted mri of the breast: potential for lesion characterization. *J Magn Reson Imaging*, 15(6):693–704, 2002.

[24] EO Stejskal. Use of spin echoes in a pulsed magnetic-field gradient to study anisotropic, restricted diffusion and flow. *J Chem Phys*, 43:3597–3603, 1965.

[25] AM Uluğ and PCM Van Zijl. Orientation-independent diffusion imaging without tensor diagonalization: Anisotropy definitions based on physical attributes of the diffusion ellipsoid. *J Magn Reson Imaging*, 9:804–813, 1999.

[26] E Warner, Hans Messersmith, Petrina Causer, Andrea Eisen, Rene Shumak, and Donald Plewes. Systematic review: Using magnetic resonance imaging to screen women at high risk for breast cancer. *Annals of Internal Medicine*, 148:671–670, 2008.

[27] C Westbrook, C Kaut Roth, and J Talbot. *MRI in practice*. Blackwell Publishing, 2005.